9. OTHER THEORY AND MODELLING STUDIES

F. Serra and J.P. Bizarro (Heads), R. Coelho, F. Salzedas, J. Ferreira, P. Rodrigues, F. Nave, D. Borba

9.1. INTRODUCTION

Besides the work on theory and modelling previously presented, this chapter reports on the following areas:

- Role of magnetic reconnection processes in the dynamics and confinement of thermonuclear plasmas;
- Non-inductive current drive;
- Reconstruction of tokamak MHD equilibria.

9.2. ROLE OF MAGNETIC RECONNECTION PROCESSES IN THE DYNAMICS AND CONFINEMENT OF THERMONUCLEAR PLASMAS

9.2.1. Introduction

The following main studies were performed in 2003:

- Destabilization of metastable modes by resonant magnetic fields;
- Poloidal $\vec{E} \times \vec{B}$ velocity (V_θ^{ExB}) studies.

9.2.2. Destabilization of metastable modes by resonant magnetic fields

The stability of neoclassical tearing modes is characterised by the existence of a threshold island width below which the mode cannot be sustained by its' own free energy. The unstable regime can only be entered if an additional physical mechanism drives the mode amplitude at the rational surface beyond the equivalent threshold island width. Forced magnetic reconnection, arising from the natural tokamaks' error-field or from mode coupling, is one promising candidate to explain NTM triggering. However, this hypothesis may sometimes be contradicted by experimental evidence that shows that, the angular frequency of the NTM, by the time it is first observed in the diagnostics, does not coincide with the frequency of the driving electromagnetic mechanism.

Although it is clear that such frequency mismatch will oppose reconnection at the early linear stages of the driving process (but not prevent it), a clear comprehensive description of the evolution of the metastable NTM angular frequency evolution is less obvious. To shed these doubts and gain further insight on the physics of NTM triggering, a non-linear reduced MHD numerical code capable of describing the dynamics of generic metastable modes (of which NTMs are an example) with mode coupling effects was developed. Associating to the mode coupling strength a corresponding resonant interacting external current sheet, it was shown that metastable modes (created for instance by rf-stabilisation of unstable modes) present a complex behaviour already at the early stages of the destabilisation by the external current, specially in the presence of differential rotation between the mode and the external fields.

Figure 9.1 shows the joint time evolution of the reconnected flux at the rational surface q=2/1 and mode angular frequency. The (2,1) mode, unstable in an ohmic regime, was first stabilized by electron cyclotron current drive (ECCD) phased at the island O-point. The external driving fields have a 2.5 kHz frequency whereas the plasma at the q=2/1 flux surface is rotating at 3.4 kHz (differential rotation). One can clearly observe that, contrary to what is normally suggested, the NTM angular rotation frequency becomes that of the rotating plasma before the irreversible destabilisation (at t≈20.25 ms). This very important remark implies that, if mode coupling is to play a role on the destabilisation of some NTMs, a perfect frequency match (mode and external driving frequencies equal) should only be observed well before the mode is destabilised. Consequently, when the island width at which the mode becomes irreversibly unstable is smaller than the magnetic diagnostic resolution, mode coupling can be wrongly excluded as the triggering mechanism when there is differential rotation.

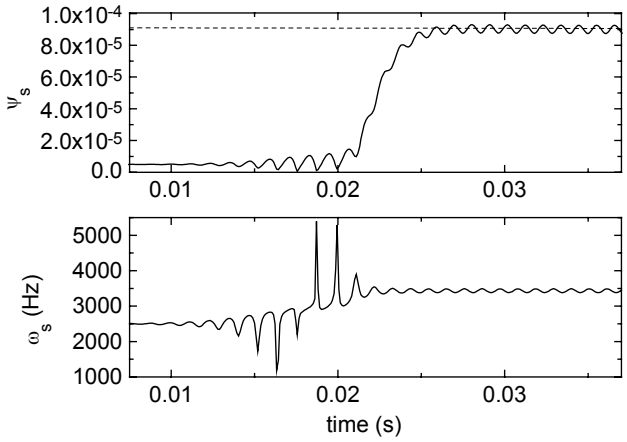

Figure 9.1 - Joint time evolution of the amplitude and frequency of a metastable modes driven by external fields with differential rotation. Mode destabilisation occurs at t≈20.25 ms.

9.2.3. Poloidal $\vec{E}\times\vec{B}$ velocity (V_θ^{ExB}) studies

There is some experimental evidence that the onset of Internal Transport Barriers (ITBs), characterised by the rapid appearance of sharp temperature gradients, is sometimes associated with magnetic activity developing around certain rational surfaces q=m/n. The resultant magnetic island topology could in principle modify the electrostatic plasma potential, thereby changing the plasma electric drift velocity in the poloidal direction (V_θ^{ExB}). Considering that an accepted criteria for reducing the typical scale length of turbulence is that $dV_\theta^{ExB}/dr > \gamma_t$, where γ_t is the typical growth rate of turbulence, a local increase in the shear of V_θ^{ExB} should favour the onset of ITBs.

It was investigated whether this magnetic activity at rational q=m/n surfaces could modify, locally, the V_θ^{ExB} plasma velocity in a sufficient and favourable way. This velocity depends, amongst others, on the equilibrium toroidal plasma velocity (V_ϕ), i.e. $V_\theta^{ExB} = V_\phi \frac{B_\theta}{B} + \frac{1}{en_i Z_{eff} B}\left[\partial p/\partial r - K\partial T_i/\partial r\right]$, where K is a geometrical function, T_i, n_i and p are, respectively, the ion temperature and density and the plasma pressure and B is the total magnetic field. Reduced MHD numerical simulations (in a cylindrical geometry) on the driven magnetic reconnection with static helical (m=2,n=1) error-fields were performed on a plasma equilibrium with axial ("toroidal") angular rotation.

The results are summarised in Figures 9.2 and 9.3, corresponding to two limiting scenarios. When the plasma anomalous perpendicular viscosity is small (i.e. a viscous diffusion time scale (τ_V) larger than the resistive diffusion time scale (τ_R)), large gradients in the toroidal velocity profile, in vicinity of the q=2/1 surface, may result and consequently affect dV_θ^{ExB}/dr significantly (Figure 9.2). However, a large plasma rotation, resultant for instance from strong NBI power, will clearly be detrimental due to a strong attenuation of the perturbation driven by the static error-fields.

On the other hand, in the scenario where $\tau_V<\tau_R$ (Figure 9.3), although a larger electromagnetic toroidal braking torque is expected, this torque will also be distributed over a larger region, resulting on a smaller effect on dV_θ^{ExB}/dr. Therefore, it was concluded that anomalous plasma viscosity and differential rotation between the error-field and the plasma at the rational surface in the plasma play an important role on the attenuation of V_{ExB}^θ shear, opposing ITB formation, in agreement with some JET observations.

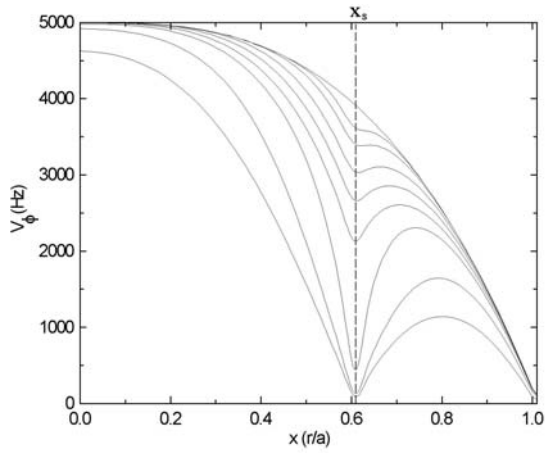

Figure 9.2 – Time evolution of the toroidal plasma velocity profile under braking by static error fields in a viscosity subdominant scenario. The $q(x_s)=2/1$ rational surface is indicated by the dashed line.

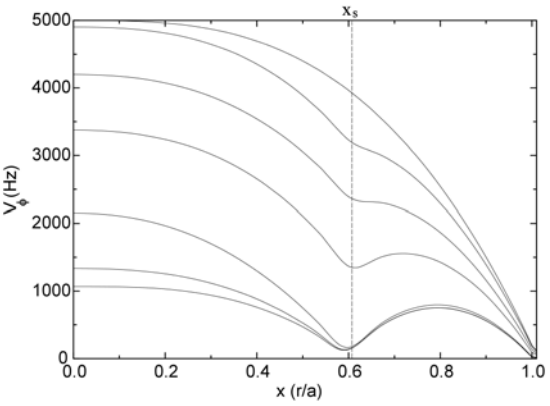

Figure 9.3 – Time evolution of the toroidal plasma velocity profile under braking by static error fields in a viscosity dominated scenario. The $q(x_s)=2/1$ rational surface is indicated by the dashed line.

9.3. NON-INDUCTIVE CURRENT DRIVE

9.3.1. Introduction

This research line included in 2003 the following main tasks:

- Computation of the wave field across a caustic, in the framework of geometrical optics;
- Study of the spectral-gap problem for Lower Hybrid (LH) current drive;
- Design of the ITER-like lower hybrid launcher[1].

9.3.2. Wave-field across a caustic

The new solution has been applied to the LH electrostatic dispersion relation. Such solution, once expanded in the

[1] Work performed in collaboration with the Association EURATOM/CEA.

"distance" from the caustic (measured in the time-like variable that parametrizes the ray equations) contains the usual first-order singularity but retains other non-singular terms that are shown to be essential to have a more correct matching of the field solutions before and after the caustic.

9.3.3. Spectral-gap problem for LH current drive

Progress has been made with the formulation of a model and the development of a computer code that confirmed numerically previous analytical studies on the magnetic ripple and toroidal effects on LH wave propagation in toroidal plasmas.

9.3.4. ITER-like lower hybrid launcher

The major objective was to optimise the design of the new ITER-like lower-hybrid launcher that is based on the Passive-Active Multijunction (PAM) concept and is to be installed at Tore Supra. Therefore, this optimisation was carried out for the key components in what their rf and coupling properties are concerned. Accordingly, the bijunction was optimised in length by determining the scattering matrix and the coupling properties in terms of: directivity, reflection, refraction index in the parallel direction, and electric field. Subsequently, again with recourse to the coupling properties, it was optimised relative to the following parameters at the mouth of the bijunction: plasma density, plasma density gradient and vacuum gap. An entire multijunction module made up of three rows of such bijunctions juxtaposed vertically, including the input linear (poloidal) taper and step (toroidal) taper, as well as the appropriate structure of output phase shifters was then modelled. The TE_{10} to TE_{30} mode converter, designed to couple the TE_{10} mode coming out of the transmission line to the TE_{30} mode required at the input of the PAM, was added next and the resulting structure, PAM+(mode-converter), was optimised in terms of: the shape of the antenna's mouth in the poloidal as well as the toroidal direction, the length of the waveguide that couples the mode converter to the PAM, and the losses due to the use of copper walls. This study lead to the conclusion that the properties of the antenna could be improved if the mode converter (inherited from the previous antenna, the C3) was somewhat altered by increasing the length of the straight section coupling it to the PAM, thus, forcing to redesign the PAM itself, given that the mode converters were by then already commissioned and could not be altered. Consequently, a good part of the study carried out until then had to be performed once more for the new design. The antenna with this last geometry was then characterised in terms of its scattering matrix and the design validated by the above study was finally called for tender, its delivery being expected for the second half of 2005. Figure 9.4 presents the radiated spectrum, whereas Figure 9.5 shows the electric-field distribution inside the antenna.

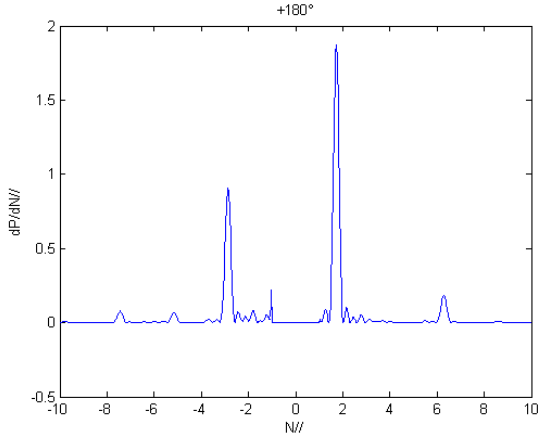

Figure 9.4 – Radiated power spectrum.

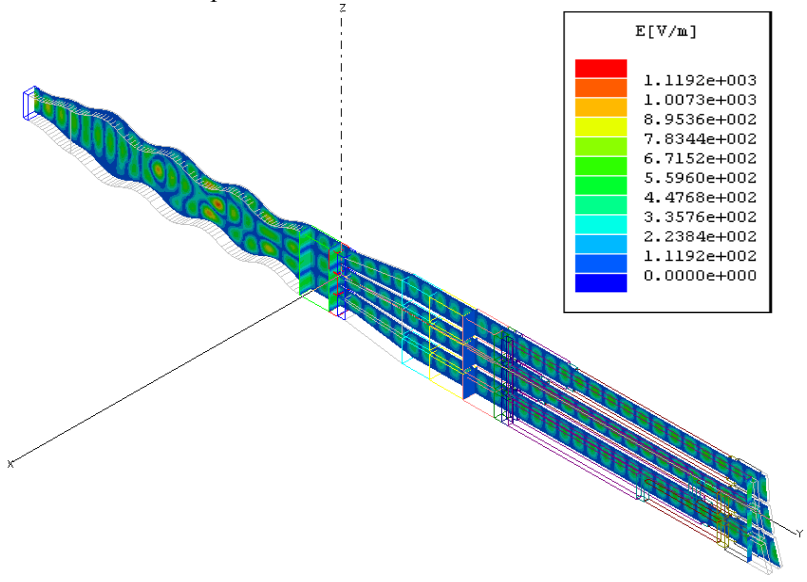

Figure 9.5 – Electric-field distribution inside the antenna.

A study similar to the one described above was also carried out for the LH antenna presently in operation at Tore Supra, the C3, although necessarily not so thorough. This antenna, which is based on the multijunction concept, precursor of the PAM, lead to a much more complex device and consequently to a more involved sub-structure model. Still, this will pave the way for the studies that are scheduled to follow next year aiming at the development of appropriate codes to characterise the behaviour of the PAM launcher when facing the plasma, and in so doing creating very important tools for the analysis of experiments.

A new code was also developed to study the stability of the ensemble multijunction + mode-converter to changes in its output reflection coefficients (in both amplitude and phase) in terms of: the total reflection coefficient at the input port, the transmitted electric field, and the total electric field at each output port (all in amplitude and phase).

9.4. RECONSTRUCTION OF TOKAMAK MHD EQUILIBRIA

9.4.1. Introduction

The following main tasks were made in 2003:

- Development of a new perturbative method to avoid the drawbacks of iterative approaches;
- Illustration of the method with ASDEX-Upgrade data.

9.4.2. Perturbative method for reconstruction of tokamak MHD equilibia

Accurate and robust equilibrium reconstruction from a set of experimental parameters is a key issue for several applications in tokamak plasmas, ranging from data analysis for toroidal-current profile fitting, transport, and mode-stability studies, to the modelling of radio-frequency wave propagation. Since external magnetic data by itself is not sufficient to establish the equilibrium, conventional approaches for reconstruction usually rely on polynomial models. These describe two independent inner profiles as, for example, the plasma pressure $p(\psi)$ and the poloidal-current flux $F(\psi)$, in terms of the poloidal-field flux ψ. The unkown polynomial coefficients are then to be found by fitting both the external magnetic data and some inner information, like the magnetic-field pitch angle $\gamma(\psi)$, through an iterative minimization of the difference between measured and computed quantities. Though accuracy may be increased by raising the order of the polynomials considered, the computational burden posed by multi-parameter fitting algorithms soon puts a limit to the computation speed, which is crucial to real-time equilibrium reconstruction.

To avoid the drawbacks of iterative approaches, a new perturbative method was devised which takes as input the plasma pressure $p(r,\theta_P)$ and the poloidal field $B_\theta(r,\theta_B)$, measured in laboratory coordinates along the chords $\theta=\theta_P$ and $\theta=\theta_B$ crossing the magnetic axis, together with suitable boundary conditions, and which is built over three main ideas: In the first place, the quest for a transformation between laboratory and flux coordinates in parallel with the solution of the poloidal-flux distribution $\psi(r,\theta)$ was dropped, eliminating unknown metric coefficients and thus reducing the nonlinear nature of the Grad-Shafranov (GS) equation to its source term only. Secondly, both this source term and the linear GS differential operator were expanded in powers of the inverse aspect ratio ε, in a procedure already known to yield a set of coupled linear ordinary differential equations (ODE), at least for the first three orders. The ODE set was properly extended to an arbitrary order, and its set of solutions was shown to be bounded, regular, and able to be written in a closed integral form, that is, recasted as a sequence of two indefinite integrals. Finally, the relation between the zeroth-order solution and the measurable profiles, $p(r,\theta_P)$ and $B_\theta(r,\theta_B)$, was established demanding every pressure and the poloidal-flux-function perturbations to vanish over the chords $\theta=\theta_P$ and $\theta=\theta_B$, with allowance for an explicit dependence of $p(\psi,\varepsilon)$ and $F(\psi,\varepsilon)$ on the inverse aspect ratio.

The explicit dependence on ε, absent in conventional perturbative approaches demanding that p and F are functions of ψ only, cures their fundamental shortcoming when reconstructing magnetic equilibria from experimental data, as they cannot address the problem of finding a suitable zeroth-order equilibrium to start with, which after an arbitrary number of perturbations would match the measured distributions. Indeed, requiring that p and F are functions of ψ only, amounts to say that such flux functions are kept unchanged (or frozen) over each flux surface, which is labeled by ψ, even if the surfaces are being displaced with growing ε. Therefore, whenever a new perturbation is added and the set of flux surfaces is displaced, the values $p(r,\theta)$ and $F(r,\theta)$ at a given point (r,θ) in laboratory coordinates are necessarily updated, making hard to match measured and computed profiles. On the contrary, the more general dependences $p(\psi,\varepsilon)$ and $F(\psi,\varepsilon)$ concede enough freedom to tailor every perturbation for some specific purpose, including their vanishing along any chord crossing the magnetic axis. Building the zeroth-order equilibrium in order to match the measured profiles, it is then possible to keep them unchanged (over the chosen chords) for any perturbation order considered.

To illustrate the method, typical parameters of the ASDEX Upgrade tokamak were taken ($a=0.5$ m, $R_0=1.67$ m, $B_0=2$ T, $n_e(0)=6.5\times10^{19}$ m^{-3}, $T_e=T_i=2$ keV, $I_p=675$ kA) together with the profiles $p(r)=2.04\varepsilon^2[1-(r/0.8)^2]$ and $RB_\theta=0.45/(1+0.65r^2)$, where the pressure is normalized to $a^4\mu_0/\psi^2_{max}$ and the poloidal field is normalized to $\psi_{max}(aR_0)^{-1}$. Figure 9.6 presents the equilibrium, computed up to terms in ε^3, while the profiles displayed in Figure 9.7 readily shows that an accurate polynomial description would require two parameters for $p(\psi)$ and three for $F(\psi)$,

being followed in due course by a computationally expensive fitting procedure with five free parameters.

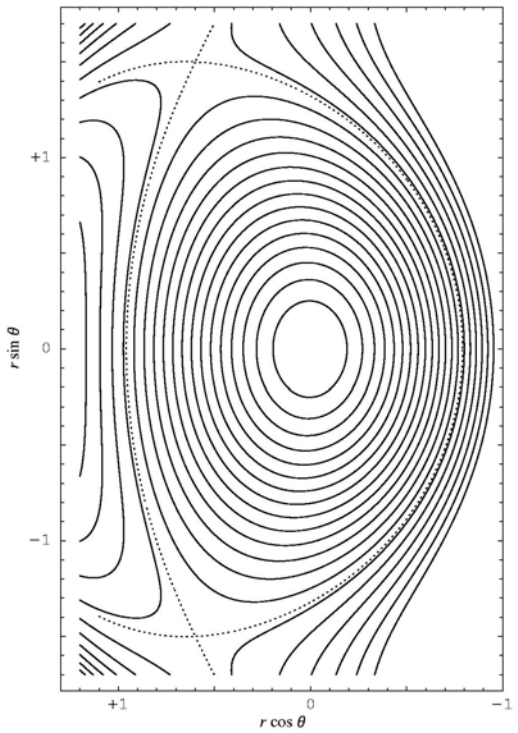

Figure 9.6 - Contours of $\psi(r,\theta)=i/15$ for $i=1,...,20$ (solid lines) and the separatrix (dotted line).

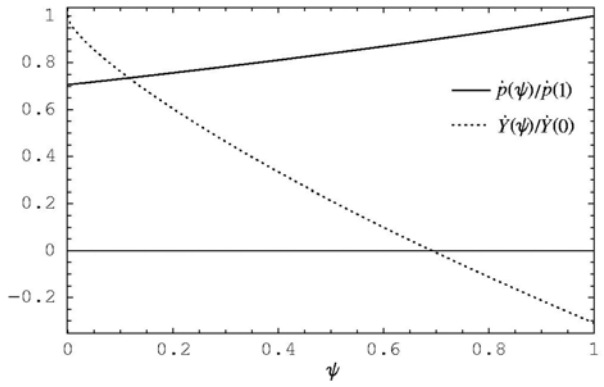

Figure 9.7 - Scaled profiles $p(\psi)/p(1)$ (solid line) and $Y(\psi)/Y(0)$ (dotted line) versus the poloidal-flux function ψ.